



OPEN

SUBJECT AREAS:

METAMATERIALS

TERAHERTZ OPTICS

SUB-WAVELENGTH OPTICS

OPTOELECTRONIC DEVICES AND
COMPONENTS

Received

24 June 2013

Accepted

7 August 2013

Published

22 August 2013

Correspondence and
requests for materials
should be addressed to
J.S.L. (jsliu4508@vip.
sina.com)

Experimental verification and investigation of disks scattering slab modes in metal-dielectric heterostructures

Lan Ding^{1,2}, Ke Jia Wang¹, Wei Wang¹, De Feng Zhu¹, Chao Yun Yin¹ & Jin Song Liu¹

¹Wuhan National Laboratory for Optoelectronics, School of Optoelectronic Science and Engineering, Huazhong University of Science and Technology, Wuhan 430074, China, ²School of Physical Science and Technology, Yunnan University, Kunming 650091, China.

A thin dielectric plate can support conventional slab modes such as leaky Fabry-Perot, guided waves and radiation modes. When the plate is coated on a metallic subwavelength disk array, it can result in new confined modes, hereby named 'disks scattering slab modes' (DSSMs). By use of a terahertz time-domain spectroscopy system, we experimentally verify the existence of two types of DSSMs in terahertz range: one we refer to as highly confined disks scattering Fabry-Perot-like modes (DSFPMs) and the other as, weakly confined disks scattering radiation-like modes (DSRMs). Spectral characteristics of these confined modes are measured and numerically simulated. Particularly, based on the experimental results and a dipole-scattering model developed here, we show that the features of the DSFPMs can be tuned by changing the filling fraction of the disk array. We believe these results can make important contributions to the designs of new terahertz devices, including tunable absorbers and filters.

It is well known that surface plasmon polariton-like bound modes, namely spoof surface plasmons (SSPs), can be sustained by periodically structured metal surfaces for longer wavelengths¹⁻³. The most exciting characteristic of SSPs is that their resonant frequencies and confinement can be tuned by the geometric parameters of the metallic periodic structures. This feature has recently sparked a wealth of experimental and theoretical works, which are aiming at developing new applications, including plasmonic chips⁴, filters⁵⁻⁷, and highly sensitive imaging⁸. However, SSPs supported by freestanding plasmonic metal structures are weakly confined for most frequencies, thus their performance in some of these practical applications is unsatisfactory. In order to resolve this problem, a class of highly confined modes was proposed in infrared region, namely hybrid spoof surface plasmons (HSSPs)⁹. These modes are supported by a metal-dielectric heterostructure (MDHS) comprised of a superstrate of dielectric layer and an ultra thin perforated metal film. The two types of HSSPs are the hybridization between SSPs and Fabry-Perot (FP) modes, namely leaky SSP-FP and the hybridization between guided waves (GW) and SSPs, referred to as SSP-GW. Based on the concept of HSSPs, practical applications such as tunable absorbers and multispectral infrared imaging can be anticipated.

Unlike the heterostructures mentioned above, we fabricate a set of samples in which hole arrays are switched for complementary geometries consisting of metallic disks that are printed on one surface of a thin dielectric slab. The reflectance of these samples is measured by a terahertz time-domain spectroscopy (THz-TDS) system (details about the system are given in the Methods section) whereby an incident THz beam is normally introduced onto the non-arrayed side of the sample. The measured reflection spectra reveals several reflectance dips, that also correspond to absorption maxima, just as in the case of heterostructures with hole arrays⁹. However, these reflection dips observed here cannot be supported by HSSPs anymore because conventional SSPs do not exist in isolated metallic structures^{1,2,10}, such as disk/rectangle arrays. Moreover, the observed phenomenon differs from both reflection behaviors of metallic disk arrays without a dielectric layer¹¹ and metallic disk arrays with a dielectric layer that has a THz beam illuminating the disk arrayed surface¹². In both of the above reflectance peaks, instead of dips, are usually expected or observed. Moreover, these works show that the reflection resonances are attributed to quasi bound states¹¹ (QBS) inherent to freestanding disk arrays, or dipolar localized surface plasmons¹² (DLSPs) sustained by supported disk arrays. However, for our samples, it is clear that the reflection dips do not result from QBS, DLSPs, and HSSPs. The question then remains, how does this phenomenon arise?

In order to answer this question, we suppose a new class of confined modes, which we shall call *disks scattering slab modes* (DSSMs) originating from the interaction among the scattered fields, diffractions, and conventional



slab modes including FP, GW or radiation modes. By analyzing the measured results, we find two types of DSSMs. The first exists in lower frequencies and its resonances present a redshift behavior with increasing filling fraction of the disk arrays. The second type appears in higher frequencies and its resonances are nearly independent of the geometry of the disk arrays. In order to reveal the physical process of these new modes, we perform a numerical simulation by means of the rigorous coupled wave analysis (RCWA) method (details about the software based on RCWA are given in the Methods section). The simulated results indicate that the first type is highly confined, closely relating to the FP mode, and hence we name it, *disks scattering FP-like mode* (DSFPM), while the second type is weakly confined, relating to the radiation mode, and thus hereby referred to as *disks scattering radiation-like mode* (DSRM).

From the viewpoint of application, DSFPMs appear more interesting and valuable due to the ability to be controlled by geometrical design of the meta-surface. Hence closer attention is paid to DSFPMs than DSRMs in this work. The DSFPM mechanism is explained by developing a dipole-scattering model, which shows that this kind of resonance results from the coupling between the conventional leaky FP modes inherent to low-index dielectric layer and the multiple reflections of the ± 1 diffracted beams produced by wave scattering on the disk array. All results encountered here may find important applications in controlling THz and microwave in both spatial and spectral domains.

Results

Figure 1a illustrates a heterostructure comprised of a dielectric layer and a meta-surface such as an array of metallic circular disks, where the thickness of the dielectric layer, the diameter, and period of the disks are denoted by h_D , a , and p , respectively. We suppose that a plane THz wave illuminates the structure at normal incidence, and its polarization is parallel to the x axis. Compared to the incident wavelength, both p and a are small. In the experiment, we fabricate the heterostructure using printed circuit boards (PCB) techniques, as shown in Fig. 1. By fixing the reflection spectrum of a silver mirror as the reference, the reflectance of the samples is obtained by a THz-TDS system, as presented in Fig. 1b. The lowest available frequency of our THz-TDS for reflection mode is about 0.06 THz.

We first investigate the effects of the FR4 thickness (h_D) on reflectance, as illustrated in Fig. 2a. One can see from the figures that the existence of metal structures has a large impact on the reflection spectra when h_D is smaller than $770 \mu\text{m}$. The reflection dips and their shift are due to the presence of DSSMs, which is discussed more clearly later. We can also deduce from Fig. 2a that the interaction among the scattered fields, diffractions, and conventional slab modes decreases with increasing h_D , derived from the increasing loss of the FR4 layer. As a result, when the layer is thicker than $770 \mu\text{m}$, the excitation of DSSM is weak enough to be neglected. Accordingly, the case for $h_D = 240 \mu\text{m}$ and $h_D = 500 \mu\text{m}$ will be discussed later.

In addition to the reflection spectra, the corresponding absorption spectra are also shown as reference in Fig. 2b, e, and f. These absorbance are calculated using directly measured reflectance and transmittance. It should be noted that the lowest credible frequency of our THz-TDS for transmission mode is about 0.1 THz, which is higher than that of the reflection mode. Thus calculated absorption spectra are not accurate below 0.1 THz (the shaded areas in Fig. 2). However, one can still see from Fig. 2 that the positions of the reflection dips approximately correspond to those of the absorption peaks. As mentioned above, these dips and peaks are associated with DSSMs.

Next, we measure the reflection spectra of the samples with variable disk period p and diameter a , respectively (not displayed here). We find that the reflectance dips at DSSM's frequencies do not shift monotonically with increasing p or a . This behavior is very different from that of metallic disk arrays without any dielectric layer¹¹ or those with thick dielectric layer^{12,13}. Compared with these previous

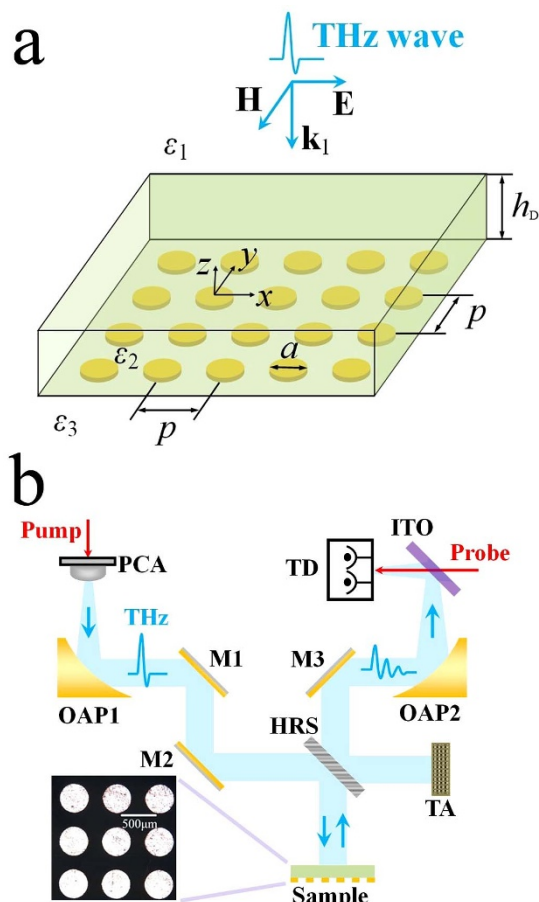


Figure 1 | The experiment. (a) Schematic of the metal-dielectric heterostructure. Note that $\epsilon_1 = \epsilon_3 = 1$ (air), $\epsilon_2 = \epsilon_{\text{FR4}}$. (b) Schematic of the experimental 'set-up'. M1, M2, and M3 are reflection mirrors. PCA is a photoconductive antenna. TA is a THz absorber. OAP1 and OAP2 are off-axis parabolic mirrors. Pump beam and probe beam are both femtosecond lasers of 800 nm with a time delay between them. The probe beam and THz beam are made collinear using ITO glass (transmits optical and reflects THz). HRS is high resistance silicon (Si). TD is a THz detector, which consists of an EO crystal, a quarter-wave plate, a Wollaston prism, and a pair of photodiodes. The inset to Fig. 1b is a microscope image of a sample corresponding to the heterostructures (bottom view). The samples are fabricated by using well-developed printed circuit boards (PCB) techniques of area about $2 \text{ cm} \times 2 \text{ cm}$ with a copper (Cu) disk array printed onto an epoxy glass-cloth laminated layer (FR4). The metallic structure is ultrathin (about $17 \mu\text{m}$) compared to incident wavelength, thus its thickness can be neglected. In addition, the dielectric permittivity of FR4 is obtained as $\epsilon_{\text{FR4}} = 4.4 + 0.35i$ through its transmittance measured by THz-TDS.

works, there are two important differences in our experiment: First, the disk array is covered with a dielectric layer, whose thickness is thin but cannot be neglected. Second, the THz wave is incident from the side of the air-FR4 interface instead of the air-disk interface. Accordingly, the reflection resonances do not lead to spectral peaks as in previous works^{10–12}, however they do produce some reflection dips, as illustrated in Fig. 2a, c, and d. Furthermore, the resonant frequencies do not shift monotonically with increasing p or a .

To clearly describe the influence of the geometric parameters of the disk array, *filling fraction* ($F = \pi a^2/4p^2$) is introduced. The THz reflectance or absorbance as a function of F is shown in Fig. 2c to f, where the cell gap ($p-a$) is fixed to $225 \mu\text{m}$. As mentioned above, there are two types of DSSMs, which lead to reflectance dips or absorbance peaks. The spectral resonances denoted by square

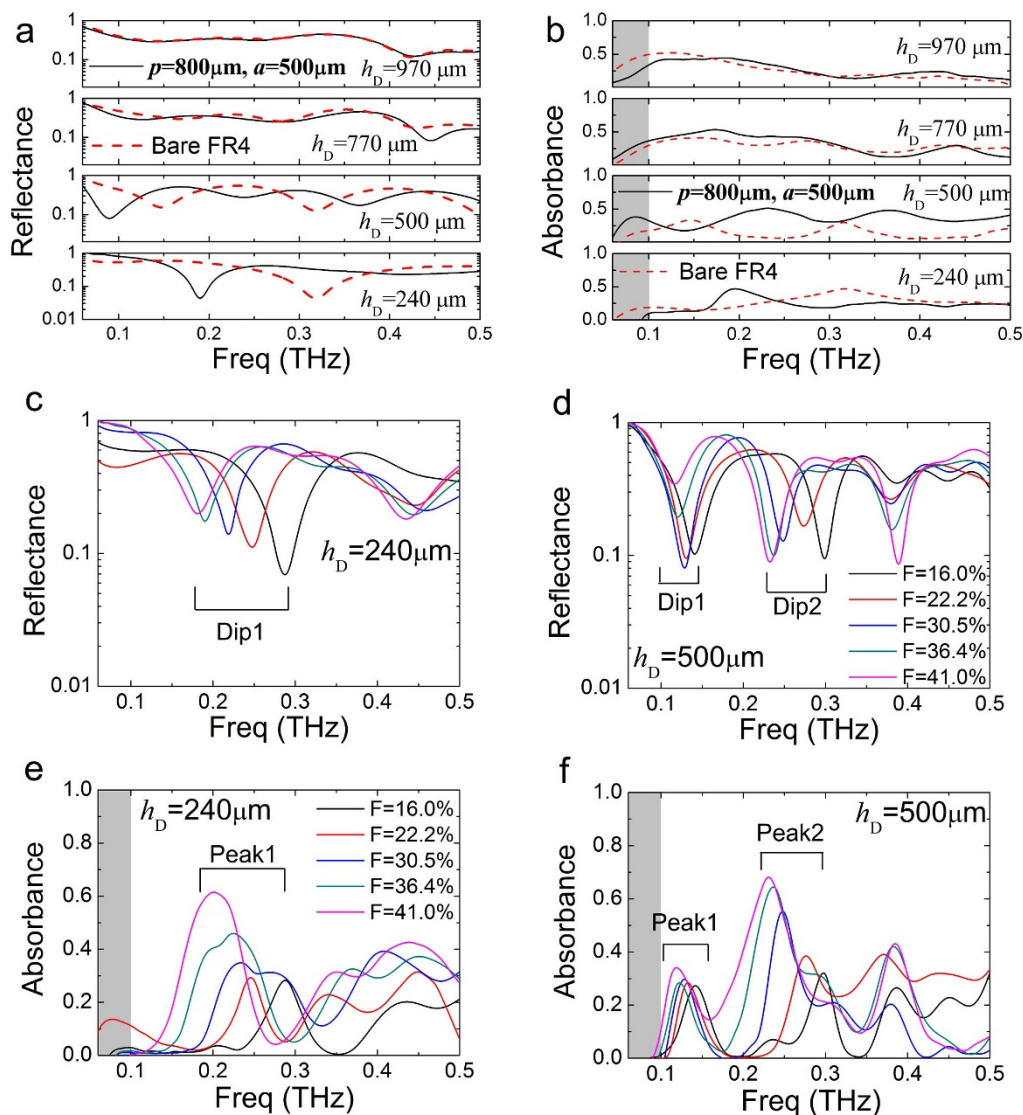


Figure 2 | The experimental results. (a, b) The effects of FR4 layer thickness on the reflection and absorption spectra. The reflection spectra of heterostructure samples (black solid curves) with h_D of 240 μm , 500 μm , 770 μm , and 970 μm are measured and compared with the spectra of corresponding bare FR4 (red dashed curves), respectively. The geometric parameters of the samples measured here are fixed to $p = 800 \mu\text{m}$, and $a = 500 \mu\text{m}$. Similar behaviour is observed for different p and a . (c, d) The filling fraction dependence of the reflection spectra of samples with $h_D = 240 \mu\text{m}$ (c) and $h_D = 500 \mu\text{m}$ (d), when cell gap ($p-a$) is fixed to 225 μm . (e, f) The absorption spectra corresponding to (c) and (d) respectively. Similar behaviour can be obtained for different $p-a$, which is not displayed here. Note that the calculated absorption spectra are not accurate below 0.1 THz.

brackets are attributed to resonant coupling to DSFPs. One can observe that these resonances are redshifted when F is increased. It means that these modes are sensitive to the geometry of the disk array, similar to the leaky SSP-FP resonances⁹. Besides, when F is larger than 22.2%, some additional resonances at higher frequencies (reflection dips or absorption peaks) can be observed at about 0.44 THz (Fig. 2c) and 0.38 THz (Fig. 2d), respectively. Similarly as in the case of SSP-GW, these resonances are not sensitive to the geometry of the metallic structure array, and we attribute them to the result of DSRMs, whose field distribution is discussed below.

Discussion

By using the RCWA method, the resonant frequencies and field distributions of the samples can be obtained. As a specific example, we present the transverse distributions of THz fields ($|H_y|$ and $|E_z|$) in one of the samples at the resonant frequencies of 0.19 and 0.43 THz, shown in Fig. 3. The two frequencies calculated through RCWA are close to the data measured in the experiment. We could infer from

Fig. 3a and b that the incident THz wave can excite a kind of highly confined mode in the MDHS at lower frequencies, such as 0.19 THz here. It is clear that the fields of this confined mode are strongly concentrated near the disk array, thus its spectral position is strongly influenced by the geometric parameters of the array. As mentioned in the experimental results, this type of highly confined mode is referred to as DSFP. In addition to DSFPs, there is another kind of weakly confined mode labeled DSRM, resulting from the interaction between the fields scattered by disks and the conventional radiation mode supported by the FR4 waveguide layer. The field distribution of DSRMs is mainly concentrated near the air-FR4 interface, shown in Fig. 3c. Therefore, the spectral positions of DSRMs are not sensitive to the geometry of the disk arrays. The numerical analysis above supports our experimental results very closely. From the viewpoint of application, the DSFPs are more interesting and valuable due to the ability to be controlled by the geometrical design of the meta-surface. Thereby the DSRMs will not be discussed in detail below.

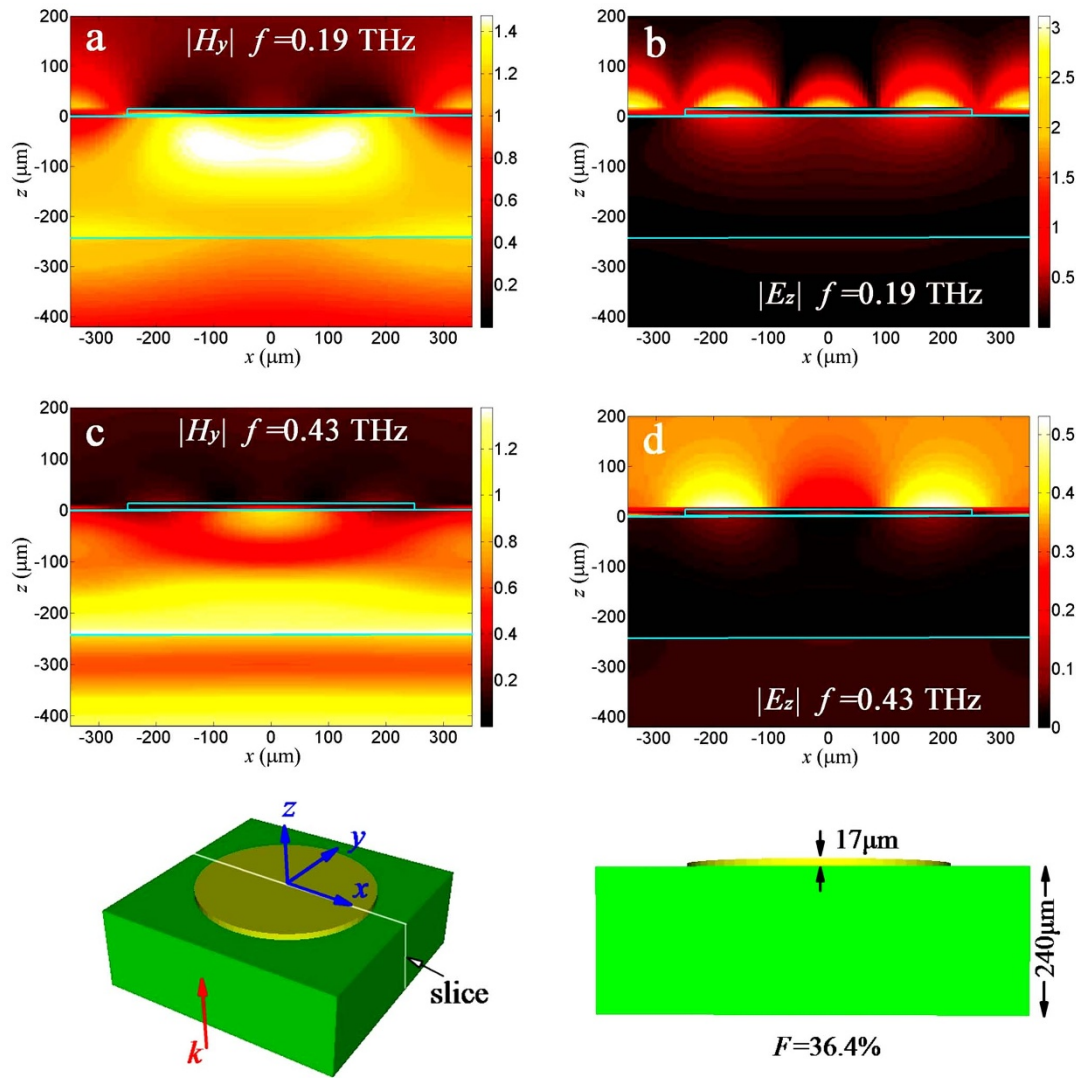


Figure 3 | Near field distribution. (a, b) The transverse distribution of the magnetic field ($|H_y|$) and electric field ($|E_z|$) for the case of $f = 0.19$ THz, which corresponds to the DSFPM. (c, d) The transverse distribution of the magnetic field ($|H_y|$) and electric field ($|E_z|$) for the case of $f = 0.43$ THz, which corresponds to the DSRM. The bottom panels display the unit cell and slice of the MDHS calculated in RCWA software. In the numerical computation, the geometric parameters are chosen as $F = 36.4\%$, $h_D = 240 \mu\text{m}$, and $p-a = 225 \mu\text{m}$.

To explain the red-shift behavior of the DSFPMs, a laconic formulation, not requiring special function evaluations, has been established by considering the MDHS as an asymmetric Fabry-Perot cavity and applying the dipole-scattering approach¹⁴. Under normal incidence, the total reflection matrix of the structure shown in Fig. 1a can be expressed as:

$$\mathbf{r}_{\text{total}} = \mathbf{r}_{12} + \mathbf{t}_{21} \mathbf{P} \mathbf{r}_{p23} \mathbf{Z} \mathbf{P} \mathbf{t}_{21}, \quad (1a)$$

$$\mathbf{Z} = [\mathbf{I} - \mathbf{P} \mathbf{r}_{21} \mathbf{P} \mathbf{r}_{p23}]^{-1}, \quad (1b)$$

where \mathbf{P} describes plane-wave propagation across the FR4 layer, \mathbf{r}_{ij} (\mathbf{t}_{ij}) is the reflection (transmission) matrix at the i th- j th medium interface, and \mathbf{r}_{p23} represents the reflection matrix of the periodic disk array. For a freestanding disk array, when the incident wavelength is commensurate with the period of the disks p (or multiple period mp) scattering of the incident wave by the disk array produces diffracted beams that are evanescent above their diffraction threshold. However, in the presence of a coated layer these evanescent diffracted beams may undergo multiple reflections in the asymmetric cavity formed between the air-FR4 interface and the array, thereby contributing to the confinement of THz wave. It should be noted that

since the external field is polarized along the x axis, the diffracted beams parallel to x are not expected to play a significant role¹⁵. Therefore, here we include some diffraction beams with parallel wave vectors $\mathbf{g}_m = (mg_1)\mathbf{y}$, in which $g_1 = 2\pi/p$ and $m = 0, \pm 1, \pm 2, \dots, \pm m_{\text{MAX}}$. Accordingly, \mathbf{r}_{ij} can be expressed as a $(2m_{\text{MAX}} + 1) \times (2m_{\text{MAX}} + 1)$ matrix with coefficients $r_{ij}^{(mm')}$, relating the incident beam m' to reflected beams m . By using Fresnel's formula¹⁶, we find

$$r_{12}^{(mm')} = \delta_{mm'} \frac{1 - \epsilon_1 k_{2z} / \epsilon_2 k_1}{1 + \epsilon_1 k_{2z} / \epsilon_2 k_1}, \quad (2a)$$

$$r_{21}^{(mm')} = \delta_{mm'} \frac{1 - \epsilon_2 k_{1zm} / \epsilon_1 k_{2zm}}{1 + \epsilon_2 k_{1zm} / \epsilon_1 k_{2zm}}, \quad (2b)$$

and the transmission matrix satisfies $t_{ij}^{(mm')} = \delta_{mm'} + r_{ij}^{(mm')}$. In Eq. (2), $k_{lzm} = \sqrt{k_l^2 - (mg_1)^2}$ ($m = 0, \pm 1, \pm 2, \dots, \pm m_{\text{MAX}}$) is the z component of the wave vector ($k_l = k_0 n_l$), where k_0 is the free-space wave vector, and n_l is the refractive-index of medium l . Moreover, the coefficients of matrix \mathbf{P} can be expressed as $P^{(mm')} = \delta_{mm'} \exp(ik_{2zm} h_D)$, respectively.



Next, applying the dipole-scattering approach, each disk can be assumed to respond with an induced dipole, thus the reflection coefficients of r_{p23} are obtained as

$$r_{p23}^{(mm')} = \frac{2\pi ik_2^2}{p^2 k_{2zm}} \left(\frac{1}{\alpha_E^{-1} - G_E} \right), \quad (3)$$

where α_E is the electric polarizability of effective dipoles, and G_E is the dipole-dipole interaction dyadic. Due to the presence of the coated dielectric layer, the electric polarizability α_E is different from that of freestanding disk array. For metals in low frequency regime, perfect electric conductor (PEC) approximation leads to simple analytical expression of the polarizability,

$$\alpha_E^{-1} = \frac{6\pi}{a^3} \frac{1 + \zeta}{\epsilon_2} - i \frac{2k_2^3}{3}, \quad (4)$$

in which ζ is deduced as $(\epsilon_2 - \epsilon_3)/(\epsilon_2 + \epsilon_3)$, which describes the asymmetric surrounding environment of the disk array. Particularly, $\zeta = 0$ means that the array of disks is placed in a homogeneous medium without coated layer or substrate. For the case of $\lambda_2 > p$ and $\lambda_2 \sim p$, another important parameter G_E reduces to

$$G_E \approx \frac{4\pi^2 \sqrt{2}}{p^3 \sqrt{\lambda_2/p - 1}} + C(\lambda_2/p) \frac{1}{p^3} + i \left(\frac{2\pi k_2}{p^2} - \frac{2}{3} k_2^3 \right), \quad (5)$$

where $C(\lambda_2/p)$ is a smooth fit to the remaining nondivergent terms¹¹. Then, based on the equations above, the zero-order coefficient $Z^{(00)}$ of the multipass matrix Z can be easily obtained. Finally, upon inspection of the denominator of $Z^{(00)}$, we can express the phase matching condition of the DSFPs in a simple form,

$$\arg\left\{ \sum_m S_m \right\}_{f=f_R} = 2q\pi, \quad (6a)$$

$$S_m = r_{21}^{(mm)} r_{p23}^{(m0)} \exp(2ik_{2zm} h_D), \quad (6b)$$

where S_m describes multiple reflections of the diffraction beam m , q is an positive integer number, and f_R is the resonant frequency of the DSFP q . To investigate the effect of m_{MAX} on the accuracy of our model, the calculation results for $m_{MAX} = 0, 1$, and 2 have been shown in Fig. 4a, in which the experimental results are also given. In fact, if only the specular beam is considered in our model ($m = m_{MAX} = 0$), Eq. (6) can be written as $\arg\{S_0\} = 2q\pi$, which is the conventional Fabry-Perot formula. Therefore it is inaccurate to neglect higher order diffraction beams, as presented in Fig. 4a. One can see from the calculation results that we can get a minimal analytical formulation with enough accuracy by fixing $m_{MAX} = 1$, which indicates that three diffraction beams with parallel wave vectors $\mathbf{g}_0 = 0$ and $\mathbf{g}_{\pm 1} = \pm (2\pi/p)\mathbf{y}$ are included in our theory. In this case, the phase matching condition of the DSFPs can be expressed as

$$\arg\{S_{-1} + S_0 + S_1\}_{f=f_R} = 2q\pi, \quad (7a)$$

$$S_0 = r_{21}^{(00)} r_{p23}^{(00)} \exp(2ik_2 h_D), \quad (7b)$$

$$S_1 = S_{-1} = r_{21}^{(11)} r_{p23}^{(10)} \exp(2ik_{2z1} h_D). \quad (7c)$$

Based on the discussion above, Eq. (7) gives us an insight into the physical mechanism of DSFPs. The multiple reflections of the specular beam (S_0) lead to a conventional FP behaviour in the heterostructure. Meanwhile, this process can receive important contributions from the multiple reflections of diffracted beams ($S_{\pm 1}$) with $\mathbf{g}_{\pm 1} = \pm (2\pi/p)\mathbf{y}$ via momentum exchange with the disk lattice. Compared to the conventional FP formula $\arg\{S_0\} = 2q\pi$, Eq. (7) gives a FP-like phase matching condition, thus the highly confined DSSMs discussed here are referred to as *disks scattering FP-like*

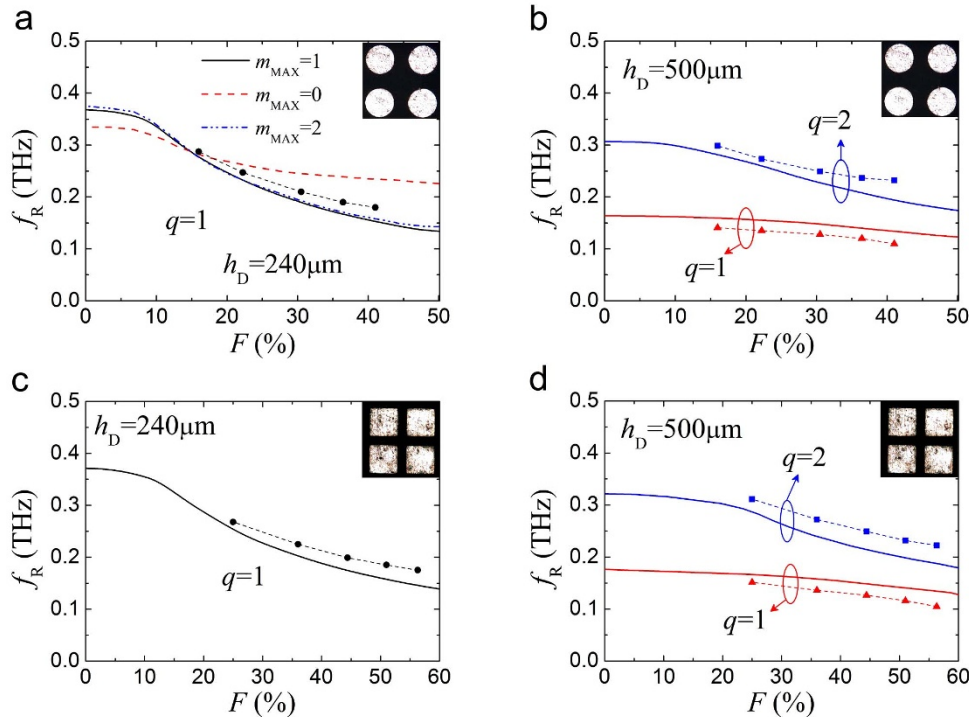


Figure 4 | The theoretical discussion. (a, b) The filling fraction dependence of the DSFP frequencies for samples shown in Fig. 1a. Note that $q = 1$ corresponds to dip 1 in Fig. 2c and d, while $q = 2$ represents dip 2 in them. (c, d) The results of metal-dielectric square patch arrays, for which the filling fraction is defined as $F = a^2/p^2$. When the disk array on the bottom of the sample is replaced by square patch array, the real part of $(\alpha_E)^{-1}$ should be changed, and an analytical expression similar to Eq. 4 is unavailable. However, we can still estimate that $\text{Re}\{(\alpha_E)^{-1}\} \propto a^{-3}(1 + \zeta)/\epsilon_2$. The insets to **Fig. 4** are microscope images of unit cells of the samples (bottom view). In all figures, the theoretical results are represented by solid lines, and the experimental results are denoted by dashes and symbols. Note that the cell gap ($p-a$) is fixed to 225 μm in these discussion.



modes (DSFPMs). It should be noted that there are also contributions from higher order diffracted beams due to scattering in this physical process, but these contributions are insignificant and thus can be neglected. Furthermore, if the disk arrays in the MDHS are replaced with hole arrays, we could extend our theory to the case of HSSPs by applying Babinet's principle¹⁴ to r_{p23} . Then the HSSP phase matching condition obtained in Ref. 9 can be replaced by a similar form.

Through Eq. (7), we calculate the resonant frequencies of the DSFPMs with increasing F for the case of $h_D = 240 \mu\text{m}$ and $500 \mu\text{m}$, respectively. These theoretical results are compared to the experimental data as shown in Fig. 4a and b. It is clear that the changing tendency of the theoretical prediction is in accordance with the measurement. Particularly, for $h_D = 240 \mu\text{m}$, experimental data and theory are closely matched. Meanwhile, we also find that the prediction of our model is not accurate for relatively larger filling fractions. This is because the dipolar scattering theory used to obtain r_{p23} does not work well when the size of the array is far away from the subwavelength limit. Moreover, if multipole approximation and complete diffraction beams^{9,15} are incorporated into the model, the accuracy of prediction can be improved, but a particularly complicated formulation will be encountered.

Furthermore, we can deduce from Fig. 4a and b that the DSFPMs of $q = 1$ is the dominant factor in the resonance-shift behavior for $h_D = 240 \mu\text{m}$, while the modes of $q = 1$ and 2 are predominant for the case of $h_D = 500 \mu\text{m}$. Upon inspection of equation (7), one finds that the phase matching condition is determined not only by r_{p23} but also by r_{21} and P_2 , thus the effect of $(1/\alpha_E - G_E)^{-1}$ on r_{total} decreases, which is different from the case of freestanding disk arrays ($r_{\text{total}} = r_{p23}$). Therefore, the resonant frequencies do not shift monotonically with increasing a or p as previous works^{6,11,13}, and the introduction of F is suitable here to describe the additional phase caused by the array-dielectric interface. Finally, we extend the investigation to the case of metal-dielectric square patch array, as shown in Fig. 4c and d, which support our previous analysis well. Based on the discussion above, the experimental results are explained, and the existence of DSSMs is demonstrated.

It is well known that lattice modes can exist in metallic nanodisk arrays and will hybridize with the localized surface plasmons (LSPs) sustained by each of the metal disks^{17–20}. However, such hybridized modes are totally different from DSFPMs, because in the THz regime real plasmons, including LSPs, do not exist in the metal disks, which are usually treated as PEC disks for THz wave. Meanwhile, the presence of the FR4 layer can also suppress the so called lattice modes supported by the disk arrays. In addition, it should be noted that a new class of hybridized confined modes, i.e. LSP-FP modes, sustained by an isolated nanoparticle-cavity system, have been reported in the visible range recently²¹. Although both of LSP-FP modes and DSFPMs are highly confined FP-like modes, LSP-FP modes can either enhance or suppress the scattering intensity slightly while DSFPMs can strongly suppress the reflectance.

In summary, we have experimentally and theoretically demonstrated that a heterostructure, comprised of a dielectric layer and a metallic subwavelength disk array, can support a new class of confined modes, namely disks scattering slab modes, in THz domain. These modes originate from the interaction among the scattered fields, diffractions, and conventional slab modes such as FP or radiation modes. Thus they include two types: DSFPMs and DSRMs. Particularly, the DSFPMs are highly sensitive to the geometry of the disk arrays, and their resonances are redshifted when the array's filling fraction is increased. Based on these results, new THz applications in spatial and spectral control can be expected, such as tunable absorbers and filters.

Methods

The experimental setup used in this work is based on a commercial THz-TDS system, which is known as Z3. It measures far-infrared spectra between 0.06 THz to

3.5 THz (reflection mode). The peak dynamic range is greater than 70 dB. The system is pumped using a pulsed fiber laser with a central frequency at 800 nm, average power of 100 mW and a pulse width of 100 fs. Oscillators with up to 1 W average power can improve system performance by as much as 20 dB. The laser beam is split into a pump and probe beam used for THz wave generation and detection. A photoconductive antenna (fabricated on a LT-GaAs wafer) is used to generate THz waves. The time delay between the pump and probe is controlled by dual retro-reflectors driven by a servo. In the THz detector, the probe beam travels collinearly with the THz beam in the EO crystal, where the probe beam is modulated by the electric field of the THz radiation via an electro-optic effect. A quarter-wave plate, a Wollaston prism and a pair of photodiodes are assembled for the balanced detection of the probe beam.

The experimental samples are designed through Protel 99SE, and fabricated by PCB techniques. We monitor and measure the geometric parameters of the samples by using of a metaloscope. Before the THz reflection experiment, each of the samples is cleaned by acetone. From the reflected/transmitted waveforms measured directly by the THz-TDS, we obtain the reflection/transmission spectra of all samples by using Fourier transformation. All measurements are performed with dry air purging (0.5% humidity). The absorbance is calculated through these measured results, and then corrected by removing the baselines. Note that the lowest available frequency of our THz-TDS for transmission mode is about 0.1 THz, which is different from that of reflection mode, thus the calculated absorption spectra are not credible below 0.1 THz.

To obtain the resonant frequencies and near field distributions of the MDHS samples, the commercially available RCWA software DiffractMOD is used. In the simulation, the permittivity of the copper disks is fixed as $\epsilon_M = -3 \times 10^4 + 10^{i2}$, while that of the FR4 layer is chosen as $\epsilon_{FR4} = 4.4 + 0.35i$. Periodic boundary conditions are imposed in x and y directions to consider periodic arrangement of the unit cells shown in the bottom panels of Fig. 3.

- Pendry, J. B., Martin-Moreno, L. & Garcia-Vidal, F. J. Mimicking surface plasmons with structured surfaces. *Science* **305**, 847–848 (2004).
- García-Vidal, F. J., Martín-Moreno, L. & Pendry, J. B. Surfaces with holes in them: new plasmonic metamaterials. *J. Opt. A* **7**, S97–S101 (2005).
- Hibbins, A. P., Evans, B. R. & Sambles, J. R. Experimental verification of designer surface plasmons. *Science* **308**, 670–672 (2005).
- Ozbay, E. Plasmonics: merging photonics and electronics at nanoscale dimensions. *Science* **311**, 189–193 (2006).
- Liu, J. S., Ding, L., Wang, K. J. & Yao, J. Q. A method to design transmission resonances through subwavelength apertures based on designed surface plasmons. *Opt. Express* **17**, 12714–12722 (2009).
- Lee, J. W., Park, T. H., Nordlander, P. & Mittleman, D. M. Optimum areal coverage for perfect transmission in a periodic metal hole array. *Appl. Phys. Lett.* **97**, 261112 (2010).
- Wang, K. J. *et al.* Theoretical and experimental research on designer surface plasmons in a metamaterial with double sets of circular holes. *Opt. Express* **19**, 11375–11380 (2011).
- Miyamaru, F., Takeda, M. W., Suzuki, T. & Otani, C. Highly sensitive surface plasmon terahertz imaging with planar plasmonic crystals. *Opt. Express* **15**, 14804–14809 (2007).
- Mousavi, S. H. *et al.* Highly Confined Hybrid Spoof Surface Plasmons in Ultrathin Metal-Dielectric Heterostructures. *Phys. Rev. Lett.* **105**, 176803 (2010).
- Takano, K. *et al.* A metal-to-insulator transition in cut-wire-grid metamaterials in the terahertz region. *J. Appl. Phys.* **107**, 024907 (2010).
- García de Abajo, F. J., Gómez-Medina, R. & Sáenz, J. J. Full transmission through perfect-conductor subwavelength hole arrays. *Phys. Rev. E* **72**, 016608 (2005).
- Lu, X. C., Han, J. G. & Zhang, W. L. Resonant terahertz reflection of periodic array of subwavelength metallic rectangles. *Appl. Phys. Lett.* **92**, 121103 (2008).
- Xiao, S. H. & Mortensen, N. A. Surface-plasmon-polariton-induced suppressed transmission through ultrathin metal disk arrays. *Opt. Lett.* **36**, 37–39 (2011).
- García de Abajo, F. J. Colloquium: Light scattering by particle and hole arrays. *Rev. Mod. Phys.* **79**, 1267–1290 (2007).
- Auguie, B., Bendaña, X. M., Barnes, W. L. & García de Abajo, F. J. Diffractive arrays of gold nanoparticles near an interface: Critical role of the substrate. *Phys. Rev. B* **82**, 155447 (2010).
- Zhang, K. Q. & Li, D. J. *Electromagnetic Theory for Microwaves and Optoelectronics* (Springer, Berlin, 1998).
- Antosiewicz, T. J. *et al.* Oscillatory Optical Response of an Amorphous Two-Dimensional Array of Gold Nanoparticles. *Phys. Rev. Lett.* **109**, 247401 (2012).
- Weick, G. *et al.* Dirac-like Plasmons in Honeycomb Lattices of Metallic Nanoparticles. *Phys. Rev. Lett.* **110**, 106801 (2013).
- Wu, S. *et al.* Enhanced Rotation of the Polarization of a Light Beam Transmitted through a Silver Film with an Array of Perforated S-Shaped Holes. *Phys. Rev. Lett.* **110**, 207401 (2013).
- Lawrie, B. J., Evans, P. G. & Pooser, R. C. Extraordinary Optical Transmission of Multimode Quantum Correlations via Localized Surface Plasmons. *Phys. Rev. Lett.* **110**, 156802 (2013).
- Schmidt, M. A. *et al.* Hybrid nanoparticle-microcavity-based plasmonic nanosensors with improved detection resolution and extended remote-sensing ability. *Nat. Commun.* **3**, 1102 (2012).



22. Wilk, R., Vieweg, N., Kopschinski, O. & Koch, M. Liquid crystal based electrically switchable Bragg structure for THz waves. *Opt. Express* **17**, 7377–7382 (2009).

Acknowledgments

This work was supported by the National Natural Science Foundation of China under Grant No. 10974063 and 61177095, Hubei Natural Science Foundation under grant No. 2010CDA001, Ph.D. Programs Foundation of Ministry of Education of China under grant No. 20100142110042, and the Fundamental Research Funds for the Central Universities, HUST: 2011TS001, 2012QN094, and 2012QN097. The authors acknowledge the help of Mr. Faraz Maani who gave a proof-reading to the manuscript with us.

Author contributions

L.D. and K.J.W. have the same contribution to this work. L.D. designed the experiment and developed the theoretical model. L.D., K.J.W. and D.F.Z. prepared the samples. K.J.W. and W.W. built the experimental set-up. Measurements were performed by L.D., D.F.Z., W.W., C.Y.Y. and K.J.W. The data was analyzed by J.S.L., L.D., K.J.W., C.Y.Y. and W.W. Numerical simulation was performed by L.D., W.W. and K.J.W. The corresponding author is J.S.L. and he co-wrote the paper with L.D. All authors contributed to discussions.

Additional information

Competing financial interests: The authors declare no competing financial interests.

How to cite this article: Ding, L. *et al.* Experimental verification and investigation of disks scattering slab modes in metal-dielectric heterostructures. *Sci. Rep.* **3**, 2493; DOI:10.1038/srep02493 (2013).



This work is licensed under a Creative Commons Attribution-NonCommercial-ShareAlike 3.0 Unported license. To view a copy of this license, visit <http://creativecommons.org/licenses/by-nc-sa/3.0>